Analytical Methods

How to cite: Angew. Chem. Int. Ed. **2021**, *60*, 9071 – 9077
International Edition: doi.org/10.1002/anie.202015251
German Edition: doi.org/10.1002/ange.202015251

Mass Spectrometry Imaging of Bio-oligomer Polydispersity in Plant Tissues by Laser Desorption Ionization from Silicon Nanopost Arrays

Laith Z. Samarah, Tina H. Tran, Gary Stacey, and Akos Vertes**

Abstract: *Mass spectrometry imaging (MSI) enables simultaneous spatial mapping for diverse molecules in biological tissues. Matrix-assisted laser desorption ionization (MALDI) mass spectrometry (MS) has been a mainstream MSI method for a wide range of biomolecules. However, MALDI-MSI of biological homopolymers used for energy storage and molecular feedstock is limited by, e.g., preferential ionization for certain molecular classes. Matrix-free nanophotonic ionization from silicon nanopost arrays (NAPAs) is an emerging laser desorption ionization (LDI) platform with ultra-trace sensitivity and molecular imaging capabilities. Here, we show complementary analysis and MSI of polyhydroxybutyric acid (PHB), polyglutamic acid (PGA), and polysaccharide oligomers in soybean root nodule sections by NAPA-LDI and MALDI. For PHB, number and weight average molar mass, polydispersity, and oligomer size distributions across the tissue section and in regions of interest were characterized by NAPA-LDI-MSI.*

Introduction

Living organisms amass, synthesize, and assimilate molecules into various classes of biopolymers that have specific biological roles. Polymers of nucleotides form the genome and the transcriptome, whereas polymers of amino acids, i.e., proteins, function as the molecular machinery of cells. Other biopolymers are less ubiquitously present and more species-specific. For example, during the interaction between soybean (*Glycine max* L. Merr.) and soil rhizobia (*Bradyrhizobium japonicum*), specialized organs, called root nodules, are formed, in which the bacteria fix atmospheric nitrogen and utilize raw material provided by the host to synthesize a special class of biopolymers, polyhydroxybutyric acid (PHB).[1,2] PHB is of physiological importance to the rhizobia, not only presenting a source of energy and carbon,[3] but its cellular levels can also strongly correlate with the redox state of the cell.[4,5] Some PHB-producing bacteria are considered candidates for the large-scale manufacture of biodegradable plastic and other polymers through processes powered by renewable energy.[6–8] For example, the Bionic Leaf 2.0 incorporates the bacteria *Ralstonia eutropha* that can reduce atmospheric CO_2 into PHB in the presence of H_2 generated from splitting water during artificial photosynthesis.[7,8]

Chemical analysis, and, in a few cases, imaging, of biopolymers have been performed using various analytical techniques, including gel permeation chromatography (GPC),[9] electrospray ionization (ESI) mass spectrometry (MS),[10,11] secondary-ion mass spectrometry (SIMS),[12] and matrix-assisted laser desorption ionization (MALDI) MS.[10,13,14] GPC is typically used to determine the molar mass distribution, polydispersity, and the degree of branching in a biopolymer,[15,16] but it requires extensive sample preparation for purification of biopolymers from their biological sources, which lowers the throughput and leads to loss of spatial information. ESI-MS is commonly used to analyze large biomolecules, including biopolymers, such as polysaccharides.[11] However, sample preparation is required prior to ESI-MS to extract and purify the biopolymers, thus eliminating the prospect of chemical imaging.[10,11]

An indirect approach based on mass spectrometry imaging (MSI) has been implemented to profile the spatial distribution for certain biopolymers by mapping the localization of the corresponding repeat unit. For example, using SIMS-MSI, the spatial distribution for lignin in plant tissues was profiled by mapping the localization of the corresponding repeat unit, guaiacyl lignin ion, at $m/z \leq 200$.[12] A similar method was used in MALDI-MSI of cutin and suberin biopolymers in plant tissues by profiling the spatial distributions for the corresponding repeat units.[17] This indirect approach can prevent the distinction between the naturally-unbound repeat units and those that are produced by in-source fragmentation of oligomers.

MALDI has been widely adopted for MSI of proteins, peptides, metabolites, and other biomolecules. However, several factors associated with the workflow in MALDI can impact the fidelity of the chemical and spatial information.[18] For example, due to the molecular complexity of biological samples, the selection of a specific matrix in MALDI can lead to preferential ionization for certain classes of biomolecules, thus limiting molecular coverage.[19] Additionally, with optimal sample preparation in MALDI using, e.g., automated matrix spraying, the original analyte spatial distribution can be preserved within lateral dimensions small enough to enable single-cell and subcellular MALDI-MSI.[20,21] For example, single Purkinje cells that interspersed the granular and molecular layers in tissue sections from mouse cerebella were distinguished on the basis of their different chemical compositions using transmission-mode MALDI-2.[21] How-

---

[*] Dr. L. Z. Samarah, T. H. Tran, Prof. A. Vertes
Department of Chemistry, George Washington University
Washington, DC 20052 (USA)
E-mail: laithsamarah@gwmail.gwu.edu
vertes@gwu.edu

Prof. G. Stacey
Divisions of Plant Sciences and Biochemistry, C. S. Bond Life Sciences Center, University of Missouri
Columbia, MO 65211 (USA)

Supporting information and the ORCID identification number(s) for the author(s) of this article can be found under: https://doi.org/10.1002/anie.202015251.

ever, suboptimal matrix deposition may lead to the spreading of analytes over the sample surface, thus potentially altering their native localization and reducing the spatial resolution.[22–24]

These limitations and others have led to efforts towards developing matrix-free MSI methods.[18] Both vacuum-based and ambient matrix-free ionization methods have been developed and successfully employed in MSI. For example, desorption electrospray ionization (DESI) and laser ablation electrospray ionization (LAESI) MS were among the ambient matrix-free ionization platforms that were successfully used to image the spatial distributions for metabolites and lipids in biological samples, e.g., tissue sections.[25,26] Vacuum-based matrix-free methods include a variety of laser desorption ionization (LDI) platforms based on inorganic substrates, such as desorption/ionization on silicon (DIOS),[27,28] graphite-assisted LDI,[29,30] nanostructure-initiator mass spectrometry (NIMS),[31,32] and silver and gold nanoparticles.[33,34] More recently, nanophotonic ionization from silicon nanopost arrays (NAPAs) has emerged as a matrix-free inorganic platform with ultra-trace sensitivity, broad molecular coverage, and molecular imaging capabilities.[35,36] For many of these inorganic platforms for LDI, the ionization efficiency can vary for different molecular classes. For example, some inorganic substrates, nanostructures and nanoparticles for LDI have been shown to favor the detection of some neutral lipids.[34,37,38]

Particular advantages of NAPA-LDI-MSI were recently demonstrated by comparing it to MALDI-MSI with respect to the ionization efficiency and spatial mapping of certain lipid classes in biological tissue sections.[38,39] NAPA-LDI-MSI was shown to enhance the ionization for particular lipid classes that are often difficult to detect using traditional organic MALDI matrices, especially in the presence of phosphatidylcholines (PCs), such as phosphatidylethanolamines (PEs) and triglycerides (TGs).[38,39] These results demonstrated the complementarity of lipid coverage between NAPA-LDI- and MALDI-MSI and gave rise to their combined application for multimodal imaging.[40]

Here, we show the detection and molecular imaging of oligomers of PHB, polyglutamic acid (PGA), and polysaccharides in soybean root nodule tissue sections using NAPA-LDI-MSI and MALDI-MSI. The two techniques exhibited strikingly different detection for the three oligomer types in the tissue. NAPA-LDI-MSI provided molecular coverage for PHB oligomers with $1 \leq n \leq 45$ repeat units and with up to ≈ 65-fold higher signal intensity compared to MALDI-MSI for root nodule sections harboring the wild-type soybean-nodulating rhizobia, *Bradyrhizobium japonicum*. For PHB, number and weight average molar mass, M_n and M_w, respectively, the polydispersity, $Đ$, and oligomer size distributions across the entire tissue section and in certain regions of interest were characterized by NAPA-LDI-MSI. Additionally, oligohexoses were detected and spatially mapped exclusively by NAPA-LDI-MSI. Conversely, MALDI-MSI outperformed NAPA in imaging PGA oligomers throughout tissue sections harboring genetically modified rhizobia defective in PHB biosynthesis (*phaC*). Our results demonstrate the complementarity between the two ionization platforms and provide insights into the regulation of PHB and PGA metabolism during symbiosis.

Results and Discussion

Analysis of PHB standard by NAPA-LDI-MS and MALDI-MS was performed to evaluate the ionization efficiency for each method. For MALDI, 2, 5-dihydroxybenzoic acid (DHB) provided the closest match between the MALDI-obtained M_n, M_w, and $Đ$ and the corresponding values provided by the vendor based on GPC data (see Table S1). Thus, mass spectra obtained from PHB standard analysis using DHB were used to compare between MALDI and NAPA. Mass spectra recorded by both techniques displayed m/z peaks separated by 86.037 Da that corresponded to the mass of the repeat unit, with the molecular formula $C_4H_6O_2$ (see Figure S1). Following the consecutive mass difference of 86.037 Da between m/z peaks in the NAPA spectrum for oligomers with $1 \leq n \leq 45$, one of the end groups was determined at m/z 124.9893, matching the adduct $[M{+}K]^+$, where M had the molecular formula $C_4H_6O_2$, and the suggested structure in Figure S1 represents M-H. Consistent with the measured monoisotopic masses of the detected oligomers, the opposite end group corresponded to a hydrogen atom (see Figure S1).

In both NAPA and MALDI spectra, the ion signal intensity decreased as the m/z increased, although the signal decline appeared faster in the NAPA spectra (see Figure S1). This inverse relationship between the ion intensity and oligomer size is likely primarily due to limitations in the production of high-mass ions by the ionization platforms and, to some degree, to reduced high-m/z analytical capabilities of the mass analyzer.

The oligomer size distributions produced by the two methods are described by the corresponding M_n, M_w, and $Đ$ (see Table S1). For NAPA and MALDI, both the M_n and M_w values were lower than the numbers generated by GPC, whereas the $Đ$ values produced by the two LDI platforms fell within the range reported by the separation method. The mismatch between the M_n and M_w values generated by the two LDI techniques and GPC can be explained by the limitations of the two ionization platforms and the mass analyzer as described above.

To assess and compare the coverage of oligomers of PHB and other biomolecules by NAPA-LDI- and MALDI-MSI in biological tissues, serial sections from soybean root nodules infected with wild-type *B. japonicum* were analyzed by both platforms.

For NAPA-LDI-MSI, the averaged spectra across an entire tissue section displayed m/z peaks that corresponded to oligomers of PHB (see Figure 1). As with PHB standard analysis, the measured m/z values for the oligomers from the tissue section were consistent with the proposed end groups. In the range $200 \leq m/z \leq 4000$, the distribution of the oligomer m/z peaks from the tissue included $1 \leq n \leq 45$ (see Figure 1). The oligomer size distribution across the analyzed tissue region was characterized by M_n, M_w, and $Đ$. In the range $200 \leq m/z \leq 4000$, the oligomer size distribution was described

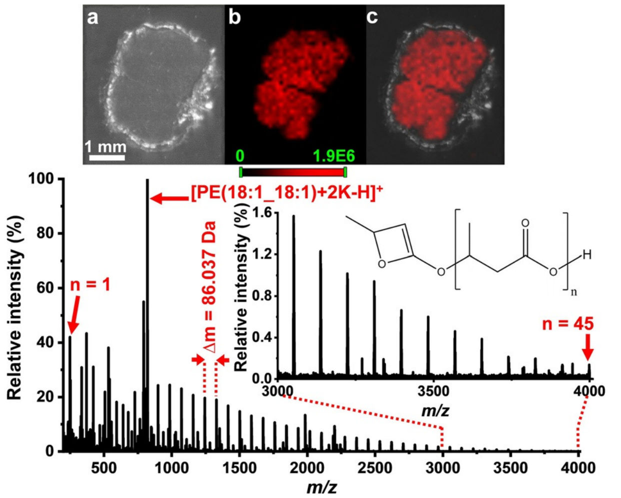

Figure 1. NAPA-LDI-MSI of soybean root nodule sections. (Top panel) a) Optical image of a 10 μm tissue section from a soybean root nodule infected with wild-type *B. japonicum*. b) Chemical image for the $[M+K]^+$ adduct of a PHB oligomer ($n=9$) ($m/z=899.3353$). c) Combined image from (a) and (b). (Bottom panel) Stitched mass spectra ($200 \leq m/z \leq 300$ and $300 \leq m/z \leq 4000$) averaged over two tissue sections show m/z peaks corresponding to oligomers of PHB (see suggested molecular structure) with $1 \leq n \leq 45$, where n is the number of repeat units. The peaks are separated by 86.037 Da, which corresponds to the mass of the repeat unit in brackets, $C_4H_6O_2$. Inset shows expanded mass spectrum in the range $3000 \leq m/z \leq 4000$.

by $M_n \approx 1043$ Da and $M_w \approx 1462$ Da (see Figure S2), leading to a polydispersity, $Đ \approx 1.40$, slightly higher than the value measured for the PHB standard.

Although NAPA-LDI- and MALDI-MS demonstrated similar detection capabilities for oligomers of PHB standard (see Figure S1), the detection and spatial mapping of the biooligomers in the tissue were significantly different for the two techniques.

To assess the molecular coverage of PHB biooligomers in biological tissues by MALDI, we analyzed soybean root nodule sections prepared with three different matrix application techniques, sublimation, spraying with an airbrush and an oscillating capillary nebulizer. Two different matrices were used, DHB and 9-aminoacridine (9-AA), and MALDI-MSI was performed in positive and negative ion modes. Additionally, as salt additives are usually used to enhance polymer ionization in MALDI-MS,[41,42] KCl and CH_3COONa were added to the matrix for imaging of some of the tissue sections. To minimize potential variations between samples that were analyzed by the different techniques, serial sections from the same root nodule were taken and analyzed by each sample preparation method for comparison.

For MALDI analysis of tissue sections sprayed with DHB using an airbrush, metabolites and lipids were detected, whereas m/z peaks that corresponded to oligomers of PHB were absent from the spectra (see Figure S3). These results were in accordance with a previous MALDI molecular tomography study in positive and negative ion modes of soybean root nodules infected with wild-type rhizobia, where automated matrix (DHB and norharmane) application was used for tissue coating.[43] Similar results were observed in our positive and negative ion mode MALDI-MSI of tissue sections sprayed with 9-AA containing salt additives using an oscillating capillary nebulizer (see Figure S4).

For MALDI analysis of tissue sections coated with DHB by sublimation, the results were surprisingly different from MALDI imaging of samples sprayed with a matrix solution. Whereas many metabolites and lipids were commonly detected and imaged by MALDI-MSI of tissue sections coated with the matrix by spraying and sublimation, oligomers of PHB were detected in the latter, although their signal intensities were significantly lower than in NAPA (see Figure S5). Similar to NAPA tissue analysis, the oligomers detected by MALDI also consisted of mainly potassium adducts with $1 \leq n \leq 21$ (see Figure S5).

Despite the demonstrated capability of MALDI in detecting and imaging oligomers of PHB from the tissue, the signal intensities for all detected PHB oligomers were significantly lower than in NAPA. The histogram in Figure 2 compares the average intensity distributions of the oligomer m/z peaks that were detected by MALDI-MSI and NAPA-LDI-MSI of 10 serial tissue sections (5 tissue sections for each method). The average signal intensities for oligomer ions with $1 \leq n \leq 21$ were ≈ 7 to ≈ 65-fold higher in NAPA spectra compared to MALDI (see Figure 2).

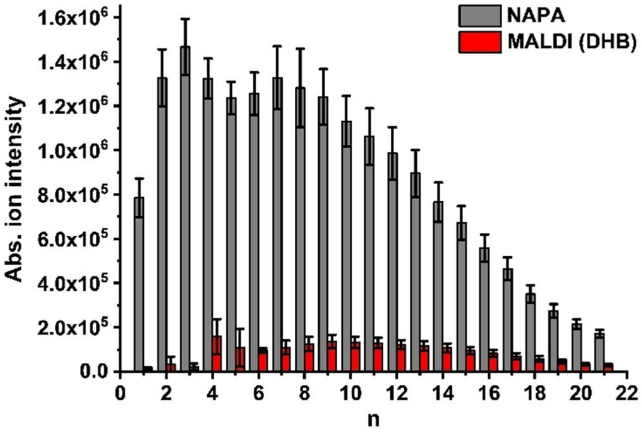

Figure 2. Comparison of average signal intensities for oligomers of PHB with $1 \leq n \leq 21$ repeat units from tissue imaging by NAPA-LDI-MSI and MALDI-MSI. Ten serial sections were used for comparison (5 for each method).

As thin (10 μm) serial tissue sections were analyzed for comparison between the two platforms, it can be assumed that the intrinsic biological variations, e.g., amounts of alkali metal ions, between the samples used in each method were insignificant. Accordingly, factors that may significantly contribute to the differences between the two techniques in the detection of PHB oligomers from the tissue include energy deposition, redistribution, mechanisms of material ejection, and the composition of the desorption plume. In MALDI, spray-based deposition of matrix droplets and sublimation yield matrix layers with different physical properties, such as surface homogeneity and crystal size.[44] The latter generally provides a more homogeneous matrix layer with smaller crystal sizes, leading to improved spot-to-spot reproducibility and higher analyte-to-matrix ratios per spot that, in some cases, may translate into raised analytical sensitivity compared to the former method.[44] Upon absorption of some of the incident photon energy, the matrix volatizes along with a relatively small amount of analytes from the tissue surface, forming a desorption plume consisting of ions and neutrals. The different physical properties of the matrix-tissue system obtained by spray-based deposition and sublimation may explain the differences in molecular coverage between the two methods for PHB oligomers as observed here and other biomolecules.[14,45]

In NAPA, the laser radiation reaches the nanoposts after penetrating the tissue, causing their surface temperature to rise sharply. Some of the thermal energy in the nanoposts is in turn transferred to the tissue on top, causing a significant amount of the tissue to volatize. In NAPA, the formation of alkali metal adducts is favored, as biological tissues often contain significant amounts of alkali metals (e.g., K). Field enhancement at the silicon nanopost tips facilitates ionization. Thus, the absence of a matrix in NAPA, combined with a significantly higher amount of desorbed material compared to MALDI, may result in the formation of higher amounts of metal adducts, including for oligomers of PHB. In a previous study, we performed MALDI-MSI of soybean root nodule tissue sections infected with wild-type *B. japonicum* using a high performance MALDI ion source fitted to a 15 Tesla FT-ICR mass spectrometer (Bruker, Daltonics).[43] In terms of the lack of PHB oligomer coverage from these tissue samples, the results were consistent with our current MSI experiments. To expand the variety of matrix deposition methods, we added another matrix application technique to this work. Using an oscillating capillary nebulizer, we obtained similar results indicating the lack of PHB coverage from the tissue. In previous work, we used a commercial sprayer (HTX TM-Sprayer), and the lack of coverage for PHB oligomers from the tissue was consistent with the MALDI-MSI results from this study.[43]

In addition to enhanced ionization of PHB oligomers from tissue sections by NAPA compared to MALDI, oligohexoses were detected and imaged exclusively by the former (see Figure S5). Characteristic of oligohexoses, m/z peaks separated by 162.053 Da (repeat unit $C_6H_{10}O_5$) were detected in the range $200 \leq m/z \leq 2000$, with $2 \leq n \leq 12$ (see Figure 3).

As PHB is considered among the essential molecules to the bacteroids during the symbiosis,[2] we investigated the potential effects that may result from the impairment of PHB biosynthesis in *B. japonicum* on the molecular composition of root nodules. Thus, root nodules formed by *G. max* infection with genetically modified rhizobia defective in PHB biosynthesis, *phaC B. japonicum*, were analyzed by NAPA- and MALDI-MSI. NAPA-LDI-MSI analysis of tissue sections from these samples indicated the absence of oligomers of PHB from the tissue, as the corresponding m/z peaks were not present in the spectra (see Figure S6).

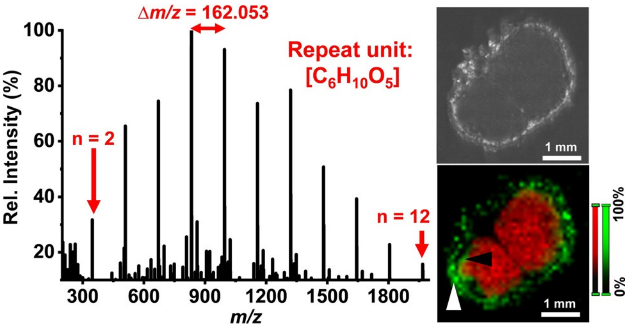

Figure 3. NAPA-LDI-MSI of oligohexoses in soybean root nodule sections. Left panel: NAPA mass spectrum taken from one pixel in the uninfected outer cortex indicated by the white arrowhead in the chemical image (bottom right panel) of a 10 μm tissue section from a soybean root nodule infected with wild-type *B. japonicum*. The spectrum shows m/z peaks corresponding to sodiated oligohexoses with $2 \leq n \leq 12$. The peaks are separated by 162.053 Da, which corresponds to the mass of the repeat unit, $C_6H_{10}O_5$, with hydrogen and hydroxyl end groups. Top right panel shows an optical image of the imaged tissue section. Bottom right panel displays the spatial distribution for a sodiated oligohexose (green) with $n=7$ in the outer (white arrowhead) and inner (black arrowhead) cortex. The spatial distribution for an oligomer of PHB with $n=11$ (red) is included for comparison with the localization of oligohexoses.

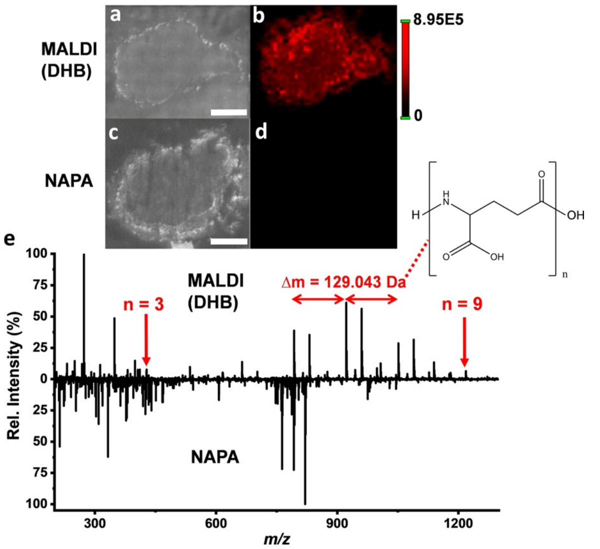

Figure 4. Comparison between MALDI- and NAPA-LDI-MSI of soybean root nodule sections infected with *phaC B. japonicum*. a,c) Optical images of 10 μm sections from soybean root nodules infected with *phaC B. japonicum*. b,d) Chemical images for protonated PGA ($n=7$) (m/z 922.3171) produced by MALDI-MSI and NAPA-LDI-MSI, respectively. e) Spectral comparison of NAPA-LDI-MSI and MALDI-MSI of root nodule tissue sections infected with *phaC B. japonicum*. The difference in mass between the peaks in the MALDI spectrum, $\Delta m = 129.043$ Da, corresponds to the repeat unit (structure shown in brackets) of PGA. The ion intensities in both images are scaled to the values displayed on the color scale. Scale bars = 1 mm.

MALDI-MSI of tissue sections harboring the mutant strain revealed the presence of new oligomers from a different biopolymer, PGA, that were not detected by NAPA (see Figure 4). In the MALDI spectra, m/z peaks separated by 129.043 Da corresponded to protonated, sodiated, and potassiated oligomers of PGA with repeat units $1 \leq n \leq 15$ in the range $200 \leq m/z \leq 2000$. In the corresponding MALDI images, oligomers of PGA distributed throughout the infection zone, inner and outer cortex of the tissue section (see Figure 4). These oligomers were absent in the spectra of root nodules infected by wild-type *B. japonicum*.

Examining the chemical images, the detected oligomers of PHB appeared localized in the infection zone, where bacteroids grew and fixed atmospheric nitrogen (see Figure 1). This is consistent with previous transmission electron microscope images that showed the presence of PHB granules inside the bacteroids.[46] To our knowledge, simultaneous chemical analysis and imaging of PHB oligomers in biological tissues has not been previously reported. Additionally, the spatial distributions for the oligomers appeared heterogeneous throughout the infection zone (see Figure 1 and Figure S7). Particularly, the oligomer ion intensities for $1 \leq n \leq 22$ appeared higher in the central region of the infection zone, and gradually dropped towards its peripheral areas (see Figure 1 and Figure S7). For example, for $n=11$ and $n=4$, the average ion intensities in the central region of the infection zone were ≈32% and ≈37% higher than in the peripheral areas, respectively (see Figure S7).

The observed spatial distributions of PHB oligomers in the NAPA images may be explained by the heterogeneity of the tissue at the cellular level. Cellular heterogeneity can manifest in varying levels of biomolecules between individual cells and has been proposed in characterizing the molecular complexity of soybean root nodules both at the tissue and single-cell levels.[43,47,48] In the infection zone, infected cells within the central region may synthesize larger amounts of PHB for better adaptation to their microenvironment. In this region, it has been shown that free oxygen levels are minimal due to diffusion resistance by the outer surrounding cell layers.[49,50] Under such conditions, PHB biosynthesis may play a more critical role in redox control in cells occupying this region.[4,51,52]

The spatial distributions of larger PHB oligomers (e.g., $23 \leq n \leq 45$) exhibited a patchy pattern throughout the infection zone, with "hot spots" that were separated by zero-intensity areas (see Figure 5). In some of the hot spots, the oligomer size distribution exhibited greater M_n than other areas in the infection zone. For example, based on the average oligomer ion intensities in regions 1 and 2 (see Figure 5), the oligomer size distributions exhibited M_n of 853 Da and 1059 Da, respectively. The difference in oligomer size distributions in certain regions may be explained by potentially different ratios of PHB biosynthesis to catabolism, and, consequently, different degree of polymerization in the bacteroids. For example, areas that exhibited relatively greater M_n for PHB oligomers (see region 2 in Figure 5) might contain bacteroids that synthesized larger oligomers for long term storage, whereas regions with lower M_n stored smaller ones that were easier to mobilize for transport.

To rule out other sources of spatial heterogeneity, Figure S8 compares the spatial distributions of PHB ($n=33$, m/z 2965.1895), an unknown ion at m/z 2200.6781, $[\mathrm{PE(16{:}0\_18{:}2)}+2\mathrm{K}-\mathrm{H}]^+$ (m/z 792.4343), and $[\mathrm{PE(34{:}1)}+2\mathrm{K}-\mathrm{H}]^+$ (m/z 794.4464), produced by NAPA-MSI in the same tissue section. This comparison indicates that the observed high intensity spots in the spatial distribution for PHB ($n=33$) are not caused by nanopost coalescence, as such intensity variations do not appear in the other chemical images shown in Figure S8. The diminishing ion intensities at higher m/z can also be excluded as an explanation because of the observed uniformity of the ion intensity distribution at m/z 2200.6781.

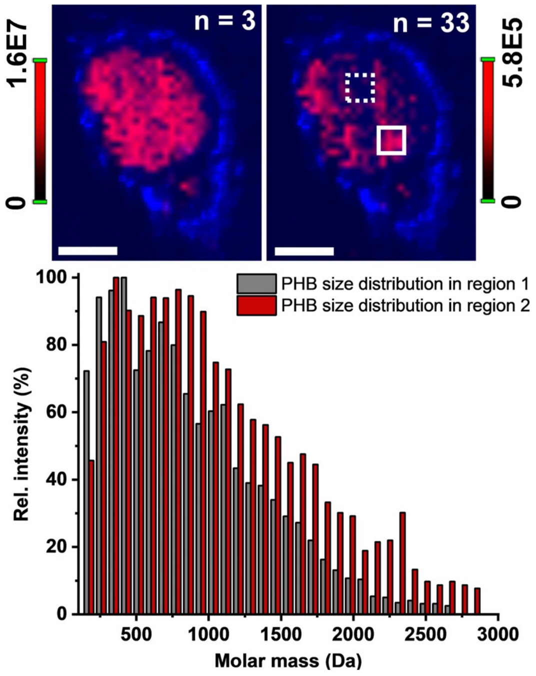

Figure 5. Oligomer size distributions for PHB with $2 \leq n \leq 33$ in two different regions of the same tissue section obtained from NAPA-LDI-MSI. NAPA images are shown for PHB ($n=3$) and PHB ($n=33$) in the same soybean root nodule tissue section infected with wild-type *B. japonicum*. Optical image of the tissue section is presented in blue. The histograms in the bottom panel display the oligomer size distributions in regions 1 (dashed box) and 2 (straight-line box) in gray and red, respectively. Scale bars = 1 mm.

Chemical images for other ions, particularly, certain lipid species, were also recorded by NAPA-MSI, revealing potential correlations between their spatial distributions and the corresponding biosynthesis sites. PEs differing in the fatty acid chain length and degree of unsaturation, as identified by tandem MS (see Figure S9), exhibited different spatial distributions (see Figure S10). For example, whereas $[\mathrm{PE(16{:}0\_18{:}2)}+2\mathrm{K}-\mathrm{H}]^+$ (m/z 792.4343) distributed in the outer cortex and infection zone, $[\mathrm{PE(18{:}1\_18{:}1)}+2\mathrm{K}-\mathrm{H}]^+$ (m/z 820.4695) was localized exclusively in the latter (see Figure S10). This suggested that PE(16:0_18:2) was likely synthesized by the plant cells as part of their membranes, and was incorporated in the symbiosome membrane,[53] a component of plant-cell origin, during cell invasion by the microsymbionts, thus appearing in both the outer cortex and infection zone. Conversely, PE(18:1_18:1) was likely synthesized by the bacteroids, thus distributing exclusively in the infection zone. Indeed, *B. japonicum* has been shown to contain large amounts of the mono-unsaturated fatty acid 18:1.[54] Additionally, different digalactosyldiacylglycerols (DGDGs) exhibited varying spatial distributions (see Figure S10). For example, whereas $[\mathrm{DGDG(34{:}3)}+\mathrm{K}]^+$ (m/z 975.5467) distributed in the infection zone, inner and outer cortex, [DGDG(18:3_18:3)+Na]$^+$ (m/z 959.5734) was observed in the latter only (see Figure S10). DGDGs are known to be localized in chloroplast membranes in plants under normal growth conditions, and can become components of the cell membrane during phosphorus deprivation.[55] Thus, the localization of DGDGs in the infection zone, inner and outer cortex of root nodules suggests an upregulation in their biosynthesis as a means of balancing phosphorus usage for other cellular processes during nitrogen fixation, e.g., adenosine triphosphate (ATP) synthesis.[56]

The reasons behind the detection of PGA exclusively in tissue sections harboring *phaC B. japonicum*, its spatial distribution, and physiological role are not entirely clear. PGA is known to be synthesized mostly by gram-positive bacteria and a few gram-negative species,[57] but, to our knowledge, there have been no reports of PGA biosynthesis in *B. japonicum.* In some bacteria, PGA has been shown to have various physiological functions, including defense against antimicrobial peptides, providing a rich carbon source, sequestering toxic metal ions, improving the absorption of essential nutrients, biofilm formation, and protection against other adverse conditions.[57] In some symbiotic soil bacteria that interact with plants, e.g., *Bacillus subtilis*, root colonization positively correlates with PGA biosynthesis.[57,58] The detection of PGA exclusively in root nodules infected with *phaC B. japonicum* raises the possibility that PGA may be synthesized by the bacteroids as an alternative biopolymer to restore some of the biological functions of PHB, e.g., carbon and energy storage.

Conclusion

In conclusion, the complementarity between NAPA-LDI-MSI and MALDI-MSI in chemical imaging of oligomers from three different biopolymers, PHB, PGA, and polysaccharides in infected plant tissue sections was demonstrated. NAPA-LDI-MSI was shown to provide higher ionization efficiency and wider repeat unit range coverage for oligomers of PHB and polysaccharides from the tissue compared to MALDI-MSI, whereas oligomers of PGA were only imaged by the latter. Complementary application of NAPA-LDI and MALDI for MSI of biological homopolymers provides new insight into the storage of energy and molecular feedstock by various organisms. As NAPA-LDI has been demonstrated to exhibit advantages in detecting and imaging compounds that are suppressed in MALDI, e.g., PHB and neutral lipids,[38,39] the complementarity of the two platforms in MSI put forth promising applications in the biomedical and clinical areas.

Acknowledgements

This material was supported by the U.S. Department of Energy (DOE), Office of Biological and Environmental Research (OBER) under award number DE-SC0013978. Additional support was provided by University of Missouri's Gus T. Ridgel Fellowship and George Washington Carver Fellowship (B.J.A.), as well as grant no. IoS-1734145 from the National Science Foundation Plant Genome Program (to G.S.). Colonies of *phaC B. japonicum* were kindly provided by Dr. Socorro Mesa Banqueri of Consejo Superior Investigaciones Cientificas, Spain. The silicon NAPA chips were manufactured at the UC Santa Barbara Nanofabrication Facility, a part of the NSF-funded National Nanotechnology Infrastructure Network, and at the NanoStructures Cleanroom Facility.

Conflict of interest

The authors declare no conflict of interest.

Keywords: biopolymers · imaging · mass spectrometry · nanopost arrays · oligomer size distribution

[1] S. Tufail, S. Munir, N. Jamil, *Braz. J. Microbiol.* **2017**, *48*, 629–636.

[2] L. P. S. Alves, F. P. do Amaral, D. Kim, M. T. Bom, M. P. Gavidia, C. S. Teixeira, F. Holthman, F. D. Pedrosa, E. M. de Souza, L. S. Chubatsu, M. Muller-Santos, G. Stacey, *Appl. Environ. Microbiol.* **2019**, *85*, e02586.

[3] J. I. Quelas, S. Mesa, E. J. Mongiardini, D. Jendrossek, A. R. Lodeiro, *Appl. Environ. Microbiol.* **2016**, *82*, 4299–4308.

[4] P. J. Senior, G. A. Beech, G. A. F. Ritchie, E. A. Dawes, *Biochem. J.* **1972**, *128*, 1193–1201.

[5] H. Stam, H. W. Vanverseveld, W. Devries, A. H. Stouthamer, *FEMS Microbiol. Lett.* **1986**, *35*, 215–220.

[6] H. Salehizadeh, M. C. M. Van Loosdrecht, *Biotechnol. Adv.* **2004**, *22*, 261–279.

[7] C. Liu, B. C. Colon, M. Ziesack, P. A. Silver, D. G. Nocera, *Science* **2016**, *352*, 1210–1213.

[8] J. Muller, D. MacEachran, H. Burd, N. Sathitsuksanoh, C. H. Bi, Y. C. Yeh, T. S. Lee, N. J. Hillson, S. R. Chhabra, S. W. Singer, H. R. Beller, *Appl. Environ. Microbiol.* **2013**, *79*, 4433–4439.

[9] A. M. Caltabiano, J. P. Foley, H. G. Barth, *J. Chromatogr. A* **2016**, *1437*, 74–87.

[10] S. Bauer, *Front. Plant Sci.* **2012**, *3*, 045.

[11] M. J. Kailemia, L. R. Ruhaak, C. B. Lebrilla, I. J. Amster, *Anal. Chem.* **2014**, *86*, 196–212.

[12] S. Jung, M. Foston, U. C. Kalluri, G. A. Tuskan, A. J. Ragauskas, *Angew. Chem. Int. Ed.* **2012**, *51*, 12005–12008; *Angew. Chem.* **2012**, *124*, 12171–12174.

[13] D. S. Cornett, M. L. Reyzer, P. Chaurand, R. M. Caprioli, *Nat. Methods* **2007**, *4*, 828–833.

[14] J. H. Yang, R. M. Caprioli, *Anal. Chem.* **2011**, *83*, 5728–5734.

[15] R. A. Cave, S. A. Seabrook, M. J. Gidley, R. G. Gilbert, *Biomacromolecules* **2009**, *10*, 2245–2253.

[16] M. Gaborieau, P. Castignolles, *Anal. Bioanal. Chem.* **2011**, *399*, 1413–1423.

[17] D. Veličković, H. Herdier, G. Philippe, D. Marion, H. Rogniaux, B. Bakan, *Plant J.* **2014**, *80*, 926–935.

[18] L. Z. Samarah, A. Vertes, *View* **2020**, *1*, 20200063.

[19] W. J. Perry, N. H. Patterson, B. M. Prentice, E. K. Neumann, R. M. Caprioli, J. M. Spraggins, *J. Mass Spectrom.* **2020**, *55*, e4491.

[20] M. Kompauer, S. Heiles, B. Spengler, *Nat. Methods* **2017**, *14*, 90–96.

[21] M. Niehaus, J. Soltwisch, M. E. Belov, K. Dreisewerd, *Nat. Methods* **2019**, *16*, 925–931.

[22] T. Alexandrov, *BMC Bioinf.* **2012**, *13*, S11.

[23] A. R. Buchberger, K. DeLaney, J. Johnson, L. J. Li, *Anal. Chem.* **2018**, *90*, 240–265.

[24] R. J. A. Goodwin, *J. Proteomics* **2012**, *75*, 4893 – 4911.
[25] P. Nemes, A. S. Woods, A. Vertes, *Anal. Chem.* **2010**, *82*, 982 – 988.
[26] J. M. Wiseman, D. R. Ifa, Y. X. Zhu, C. B. Kissinger, N. E. Manicke, P. T. Kissinger, R. G. Cooks, *Proc. Natl. Acad. Sci. USA* **2008**, *105*, 18120 – 18125.
[27] Q. Liu, Z. Guo, L. He, *Anal. Chem.* **2007**, *79*, 3535 – 3541.
[28] J. Wei, J. M. Buriak, G. Siuzdak, *Nature* **1999**, *399*, 243 – 246.
[29] J. Sunner, E. Dratz, Y. C. Chen, *Anal. Chem.* **1995**, *67*, 4335 – 4342.
[30] S. W. Cha, E. S. Yeung, *Anal. Chem.* **2007**, *79*, 2373 – 2385.
[31] T. R. Northen, O. Yanes, M. T. Northen, D. Marrinucci, W. Uritboonthai, J. Apon, S. L. Golledge, A. Nordstrom, G. Siuzdak, *Nature* **2007**, *449*, 1033 – 1036.
[32] O. Yanes, H. K. Woo, T. R. Northen, S. R. Oppenheimer, L. Shriver, J. Apon, M. N. Estrada, M. J. Potchoiba, R. Steenwyk, M. Manchester, G. Siuzdak, *Anal. Chem.* **2009**, *81*, 2969 – 2975.
[33] N. Goto-Inoue, T. Hayasaka, N. Zaima, Y. Kashiwagi, M. Yamamoto, M. Nakamoto, M. Setou, *J. Am. Soc. Mass Spectrom.* **2010**, *21*, 1940 – 1943.
[34] S. N. Jackson, K. Baldwin, L. Muller, V. M. Womack, J. A. Schultz, C. Balaban, A. S. Woods, *Anal. Bioanal. Chem.* **2014**, *406*, 1377 – 1386.
[35] B. N. Walker, J. A. Stolee, A. Vertes, *Anal. Chem.* **2012**, *84*, 7756 – 7762.
[36] S. A. Stopka, C. Rong, A. R. Korte, S. Yadavilli, J. Nazarian, T. T. Razunguzwa, N. J. Morris, A. Vertes, *Angew. Chem. Int. Ed.* **2016**, *55*, 4482 – 4486; *Angew. Chem.* **2016**, *128*, 4558 – 4562.
[37] A. D. Feenstra, K. C. O'Neill, G. B. Yagnik, Y. J. Lee, *RSC Adv.* **2016**, *6*, 99260 – 99268.
[38] J. A. Fincher, J. E. Dyer, A. R. Korte, S. Yadavilli, N. J. Morris, A. Vertes, *J. Comp. Neurol.* **2019**, *527*, 2101 – 2121.
[39] J. A. Fincher, A. R. Korte, J. E. Dyer, S. Yadavilli, N. J. Morris, D. R. Jones, V. K. Shanmugam, R. K. Pirlo, A. Vertes, *J. Mass Spectrom.* **2020**, *55*, e4443.
[40] J. A. Fincher, A. R. Korte, S. Yadavilli, N. J. Morris, A. Vertes, *Analyst* **2020**, https://doi.org/10.1039/d1030an00836b.
[41] X. D. Tang, P. A. Dreifuss, A. Vertes, *Rapid Commun. Mass Spectrom.* **1995**, *9*, 1141 – 1147.
[42] G. Montaudo, F. Samperi, M. S. Montaudo, *Prog. Polym. Sci.* **2006**, *31*, 277 – 357.
[43] D. Veličković, B. J. Agtuca, S. A. Stopka, A. Vertes, D. W. Koppenaal, L. Paga-Tolic, G. Stacey, C. R. Anderton, *ISME J.* **2018**, *12*, 2335 – 2338.
[44] T. W. Jaskolla, M. Karas, U. Roth, K. Steinert, C. Menzel, K. Reihs, *J. Am. Soc. Mass Spectrom.* **2009**, *20*, 1104 – 1114.
[45] J. A. Hankin, R. M. Barkley, R. C. Murphy, *J. Am. Soc. Mass Spectrom.* **2007**, *18*, 1646 – 1652.
[46] H. B. Krishnan, *J. Bacteriol.* **2002**, *184*, 831 – 839.
[47] S. A. Stopka, R. Khattar, B. J. Agtuca, C. R. Anderton, L. Pasa-Tolic, G. Stacey, A. Vertes, *Front. Plant Sci.* **2018**, *9*, 1646.
[48] L. Z. Samarah, R. Khattar, T. H. Tran, S. A. Stopka, C. A. Brantner, P. Parlanti, D. Velickovic, J. B. Shaw, B. J. Agtuca, G. Stacey, L. Pasa-Tolic, N. Tolic, C. R. Anderton, A. Vertes, *Anal. Chem.* **2020**, *92*, 7289 – 7298.
[49] J. D. Tjepkema, C. S. Yocum, *Planta* **1973**, *115*, 59 – 72.
[50] J. D. Tjepkema, C. S. Yocum, *Planta* **1974**, *119*, 351 – 360.
[51] P. J. Senior, E. A. Dawes, *Biochem. J.* **1971**, *125*, 55 – 66.
[52] M. A. Trainer, T. C. Charles, *Appl. Microbiol. Biotechnol.* **2006**, *71*, 377 – 386.
[53] E. Roth, K. Jeon, G. Stacey in *Molecular Genetics of Plant Microbe Interactions* (Eds.: R. Palacios, D. P. Verma), American Phytopathological Society Press, Minnesota, **1988**, pp. 220 – 225.
[54] M. Boumahdi, P. Mary, J. P. Hornez, *J. Appl. Microbiol.* **1999**, *87*, 611 – 619.
[55] B. Essigmann, S. Guler, R. A. Narang, D. Linke, C. Benning, *Proc. Natl. Acad. Sci. USA* **1998**, *95*, 1950 – 1955.
[56] N. Gaude, H. Tippmann, E. Flemetakis, P. Katinakis, M. Udvardi, P. Dormann, *J. Biol. Chem.* **2004**, *279*, 34624 – 34630.
[57] Z. T. Luo, Y. Guo, J. D. Liu, H. Qiu, M. M. Zhao, W. Zou, S. B. Li, *Biotechnol. Biofuels* **2016**, *9*, 134.
[58] Y. Y. Yu, F. Yan, Y. Chen, C. Jin, J. H. Guo, Y. R. Chai, *Front. Microbiol.* **2016**, *7*, 1811.

Manuscript received: November 15, 2020
Revised manuscript received: December 30, 2020
Accepted manuscript online: February 2, 2021
Version of record online: March 9, 2021

Angewandte
Eine Zeitschrift der Gesellschaft Deutscher Chemiker
Chemie

Supporting Information

Mass Spectrometry Imaging of Bio-oligomer Polydispersity in Plant Tissues by Laser Desorption Ionization from Silicon Nanopost Arrays

Laith Z. Samarah, Tina H. Tran, Gary Stacey, and Akos Vertes**

anie_202015251_sm_miscellaneous_information.pdf

Supporting Information

Table of Contents

Experimental Section

Fabrication of NAPA Imaging Chips. The nanofabrication of NAPA chips has been previously described.[1-2] Briefly, high-conductivity p-type silicon wafers (Silicon Valley Microelectronics, Inc., Santa Clara, CA) were used to fabricate silicon nanoposts with post dimensions of 1100 nm in height, 150 nm in diameter, and a periodicity of 337 nm using deep ultraviolet projection lithography (DUV-PL) followed by deep reactive ion etching (DRIE).

Preparation of PHB standard for NAPA- and MALDI-MS. Poly(R)-3-hydroxybutyric acid (Polysciences, Inc., PA, USA, catalogue no. 16934), with an average molar mass of ~2000 Da and a polydispersity ($Đ$), $1.1 \leq Đ \leq 1.4$, determined by GPC, was used as a standard for analysis by NAPA-LDI-MS and MALDI-MS. For NAPA-LDI-MS, the PHB standard was dissolved in chloroform to make 0.1 mg/mL solution, and 1 μL aliquots of the resulting solution were directly deposited onto NAPA wells. After drying, 250 nL aliquots of 100 nM KCl solution in water were spotted onto the NAPA chips to facilitate ionization. For MALDI-MS, sample preparation was based on a previous protocol for MALDI analysis of purified polyhydroxyalkanoates.[3] In brief, several matrices, including sinapic acid, 2-(4-hydroxyphenylazo) benzoic acid (HABA), α-cyano-4-hydroxycinnamic acid (CHCA), 9-aminoacridine (9-AA), and 2, 5-dihydroxybenzoic acid (DHB), were tested for MALDI-MS of the PHB standard. Depending on their solubility, the matrices were dissolved in either methanol or 2:1 methanol:chloroform to form 10 mg/mL solution. A mixture of the matrix solution and 0.1 mg/mL PHB solution in chloroform was prepared in a matrix-to-standard ratio of 5:2, and acidified (0.1% formic acid) KCl solution in methanol was added to a final concentration of 100 nM. Finally, 1 μL aliquots of the resulting matrix-standard mixture were deposited onto a stainless steel MALDI plate and left to air-dry.

Polydispersity calculation. Calculation of the number average molar mass, M_n, weight average molar mass, M_w, and $Đ$ (M_w/M_n) for PHB oligomers was performed based on a previously described approach.[4] Briefly, the intensities (approximated by the peak heights) for *m/z* peaks of different adducts were summed to represent the relative abundance, A_i, of the corresponding i^{th} PHB oligomer. The resulting A_i were plotted as a function of the corresponding oligomer molar mass, M_i, to produce the oligomer size distribution observed in NAPA and MALDI. The distributions were then characterized by $M_n = \sum A_i M_i / \sum A_i$, $M_w = \sum A_i M_i^2 / \sum A_i M_i$, and $Đ = M_w/M_n$.[4] To capture the spatial variations of the PHB oligomer size distribution in the imaged tissue sections, NAPA mass spectra across the interrogated region were averaged, and A_i, M_i, M_n, M_w, and $Đ$ were determined as described above.

***B. japonicum* strains and cultures.** Culturing of wild-type *B. japonicum* USDA110 strain was fully described in a previous publication.[5] *B. japonicum* strain defective in PHB biosynthesis (*phaC*) was cultured as described previously.[6]

***G. max* growth and inoculation with *B. japonicum*.** *G. max* seed germination and plant growth were fully described in a previous publication.[5] Briefly, *G. max* seeds of 'Williams 82' were inoculated with 500 µL of a prepared solution containing either wild-type or *B. japonicum phaC* mutant cells and placed in a growth chamber (Percival E36HO, Percival Scientific, Perry, IA, USA) at 26 °C for 16 hours of light, and 24 °C for 8 hours in the dark, and relative humidity at 55 %. To avoid cross-contamination between the two different bacterial strains, the inoculated seeds were grown separately, and the growth chamber was sterilized with 50 % bleach solution and 70 %

ethanol between the two separate growth periods. Every three days, the growing plants were supplied with nitrogen-free "B & D" medium.[7]

Preparation of root nodule tissue sections for MSI. Tissue section preparation from soybean root nodules was described in a previous publication.[5] Briefly, after 21 days of growth, inoculated soybean plants were removed from the potting material and the roots were rinsed with water to remove vermiculite and perlite. The nodules were then gently removed from the roots in liquid nitrogen and stored at -80 °C to preserve the sample integrity. For MSI, root nodules were embedded in 2.5% carboxymethylcellulose (CMC) and cooled in a cryostat microtome (CM1800, Leica Microsystems Inc., Nussloch, Germany) at -18 °C until the embedding medium was frozen. Cryosections 10 μm in thickness were prepared and thaw-mounted onto NAPA imaging chips or Superfrost Plus microscope slides (Fisher Scientific, Hampton, NH, catalogue no. 12-550-15) for NAPA or MALDI analysis, respectively, and placed in a vacuum desiccator for ~ 30 minutes before analysis.

For MALDI-MSI experiments, DHB and 9-AA were used as matrices. The former was used for positive ion mode analysis, whereas the latter was used for both positive and negative ion mode analyses. Additionally, to enhance the ionization of polymers in MALDI-MSI of some of the tissue sections, potassium chloride and sodium acetate were added to the matrix solution to a final concentration of ~100 μM. The matrices were applied to the sections by sublimation or spraying, and the latter was accomplished using either an airbrush or an oscillating capillary nebulizer. Matrix spraying with an airbrush and an oscillating capillary nebulizer has been described previously.[8-9] Briefly, for coating samples with an airbrush, a Paasche airbrush TS-100D (Chicago, IL) was used to spray 100 mg/mL DHB in methanol onto the dry sections, with

20-25 cycles alternating between spraying for 10 s and a 30 s drying period. For matrix spraying with an oscillating capillary nebulizer, an Aztek A470 airbrush (Testors, Vernon Hills, IL) was modified to thread a fused silica capillary (inner diameter 100 µm) through the spray nozzle. The matrix solution, in this case, 12.5 mg/mL 9-AA in 90% methanol supplied with ~100 µM of KCl and CH_3COONa, was delivered into the capillary using a syringe (1750TLL, Hamilton Co., Reno, NV) and a syringe pump (KS100, KD Scientific, Holliston, MA). The tissue section was placed ~17 cm below the airbrush nozzle, and the matrix solution was pumped at a rate of 47 µL/min. Ultrapure nitrogen was used as the nebulizing gas at a pressure of 276 kPa (40 psi), and a total of 140 µL of the matrix solution was sprayed. For matrix application by sublimation, a Pyrex petri dish was placed in a vacuum chamber that was heated to 140 °C by immersing its base in a pre-heated sand bath. A volume of 1 mL of DHB in methanol (100 mg/mL) was added to the petri dish. The tissue sections on the microscope slides were positioned ~ 1.5 cm from the surface of the dish, and the surface of the microscope slide was cooled by placing a 10 mL glass beaker containing ice slush on the back side of the slide. The air pressure in the vacuum chamber was reduced using a vacuum pump, and the matrix was allowed to sublime for ~ 7 minutes. Alternatively, the matrix was sublimed by heating at 140 °C using the same setup without applying a vacuum.

MS data acquisition. All experiments were performed on a MALDI-LTQ-Orbitrap XL mass spectrometer (Thermo Scientific, San Jose, CA) equipped with a nitrogen laser emitting radiation at 337 nm with a repetition rate of 60 Hz, and a focal spot size of ~100 µm×80 µm. The mass resolving power was set to 30,000 for all MS experiments.

For MS analysis of PHB standard, a laser fluence of 60 mJ/cm^2 and 3 laser shots/scan were used for NAPA-LDI-MS, whereas a laser fluence of 16 mJ/cm^2 and 10 laser shots/scan were used for MALDI-MS. For both methods, due to a drop in the instrument sensitivity for acquisition over broad *m/z* ranges, the scanned ranges were divided into $275 \leq m/z \leq 2000$ and $2000 \leq m/z \leq 4000$. The low *m/z* boundary, $m/z = 275$, was selected based on high spectral interference from the matrix-related peaks below this value. The peak intensities in the high-mass range were normalized to the base peak in the lower-mass range, and the two spectra were stitched.

For NAPA-LDI- and MALDI-MSI of biological tissue sections, laser fluences of 112 mJ/cm^2 and 28 mJ/cm^2 were used, respectively, with 10 laser shots per scan for both MSI techniques. A raster step size of 100 μm was used throughout tissue imaging for both platforms. The acquisition ranges were set to $200 \leq m/z \leq 2000$, and $300 \leq m/z \leq 4000$ for capturing and imaging larger biooligomers. For MALDI-MSI in negative ion mode, the same laser fluence, number of laser shots per scan, and raster step size were used as in positive ion mode. The *m/z* range in the negative-ion mode was set to $200 \leq m/z \leq 3000$. The automatic gain control (AGC) was turned off and the injection time was set to 50 ms during all MSI experiments to keep the number of laser shots per pixel constant. Reported absolute ion intensities indicate the ion counts.

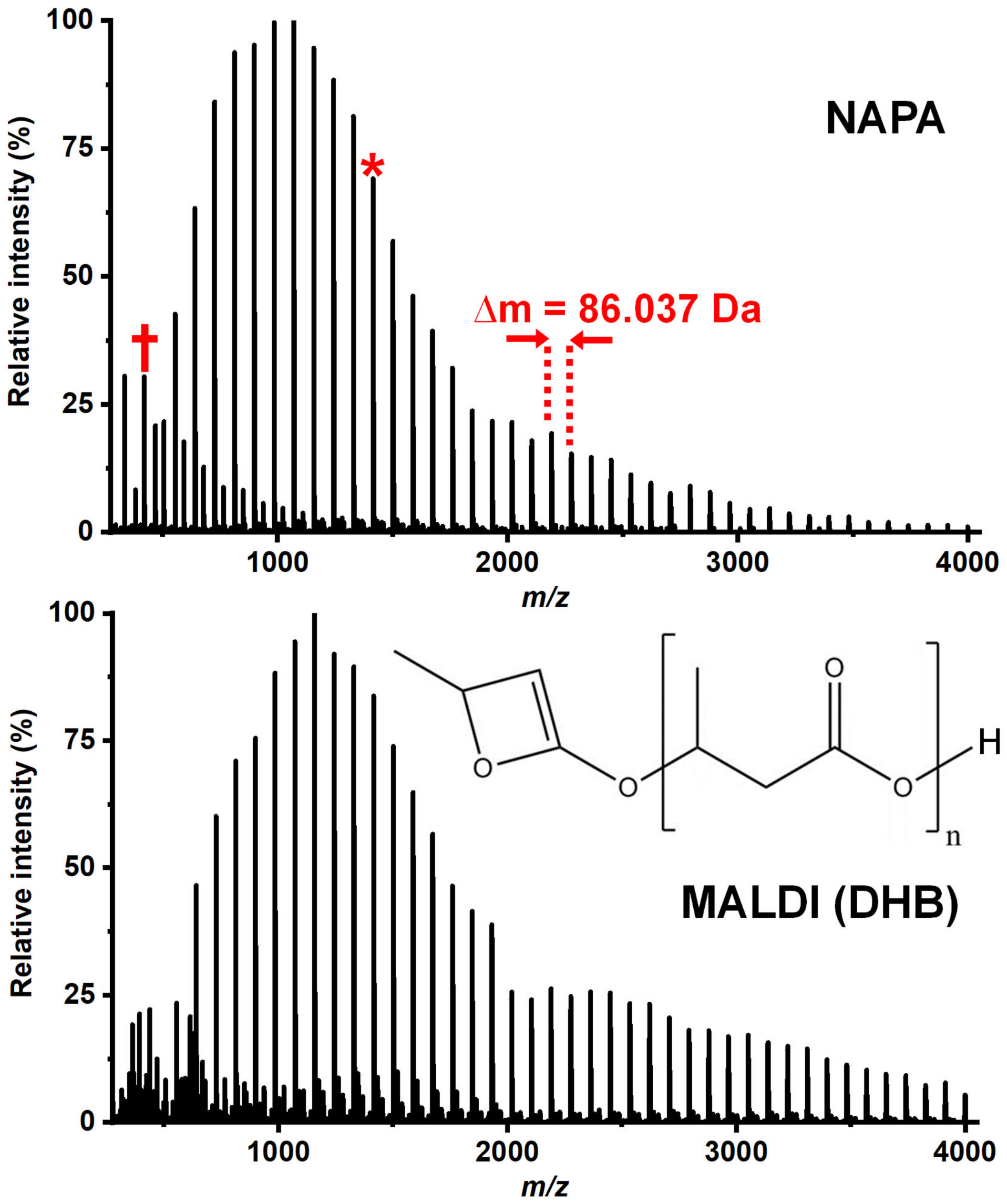

Figure. S1. Stitched mass spectra obtained from PHB standard analysis by positive ion mode NAPA-LDI-MS and MALDI-MS. Spectra were acquired in two separate *m/z* ranges, $275 \leq m/z \leq 2000$ and $2000 \leq m/z \leq 4000$. The mass difference (86.037 Da) between the *m/z* peaks corresponds to the repeat unit shown in brackets in the inset, with the molecular formula $C_4H_6O_2$. $[M+K]^+$ (*) and $[M+2K-H]^+$(†) ions were both abundant in the NAPA spectrum, whereas for MALDI, all peaks corresponded to $[M+K]^+$ and $[M+Na]^+$ adducts. The displayed molecular structure, consistent with the measured *m/z* values, shows the suggested end groups and the repeat unit in brackets, where in the *m/z* range shown above, $1 \leq n \leq 45$. The absolute ion intensities (counts) for the base peaks in the NAPA and MALDI mass spectra were 1.44×10^7 and 1.48×10^7, respectively.

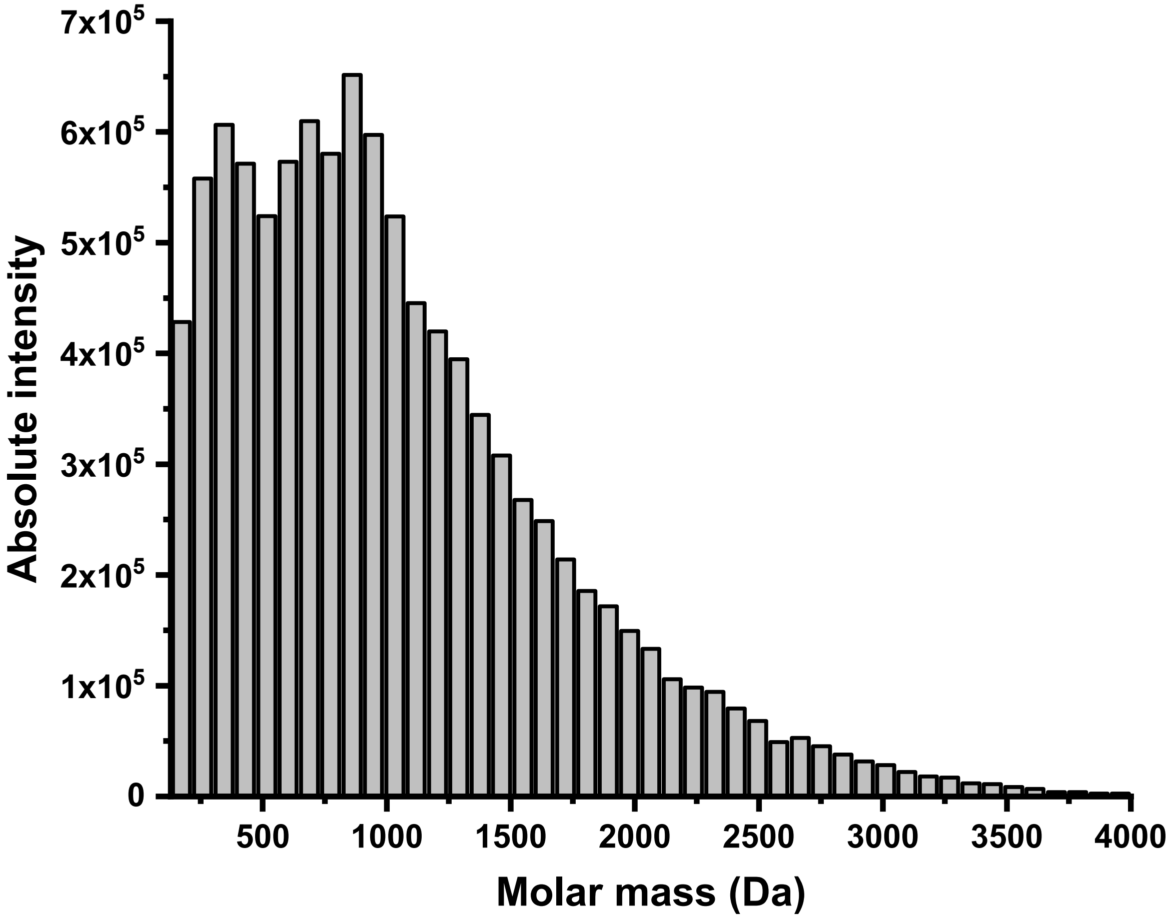

Figure S2. PHB oligomer size distribution obtained from NAPA-LDI-MSI of an entire tissue section from a soybean root nodule infected with wild-type *B. japonicum*, with $M_n \approx 1043$ Da, $M_w \approx 1462$ Da, and $Đ \approx 1.40$.

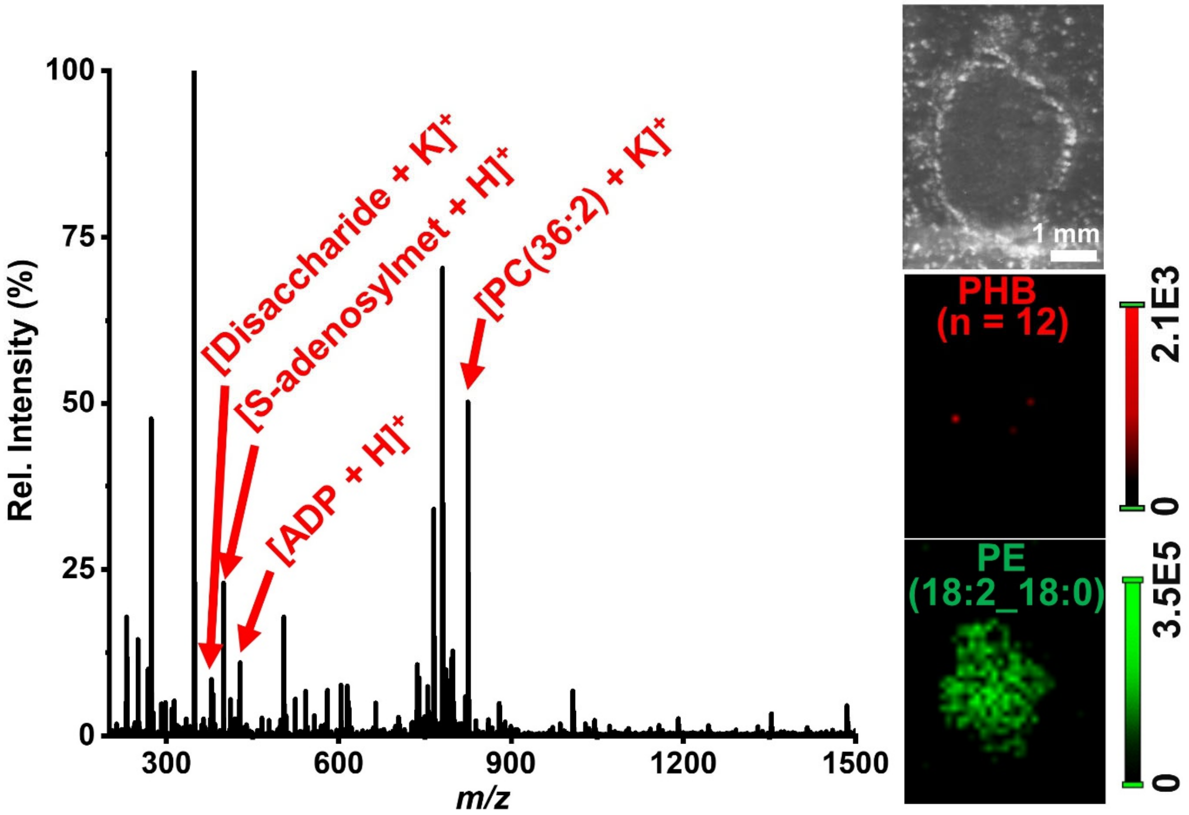

Figure S3. MALDI-MSI of a soybean root nodule tissue section infected with wild-type *B. japonicum* and sprayed with DHB using an airbrush. A representative MALDI mass spectrum is displayed with a few annotated *m/z* peaks. Metabolites and lipids were detected (see mass spectrum) and imaged (see example in bottom chemical image in right panel), whereas PHB oligomers were absent from the spectrum and the corresponding chemical image (see middle chemical image in right panel).

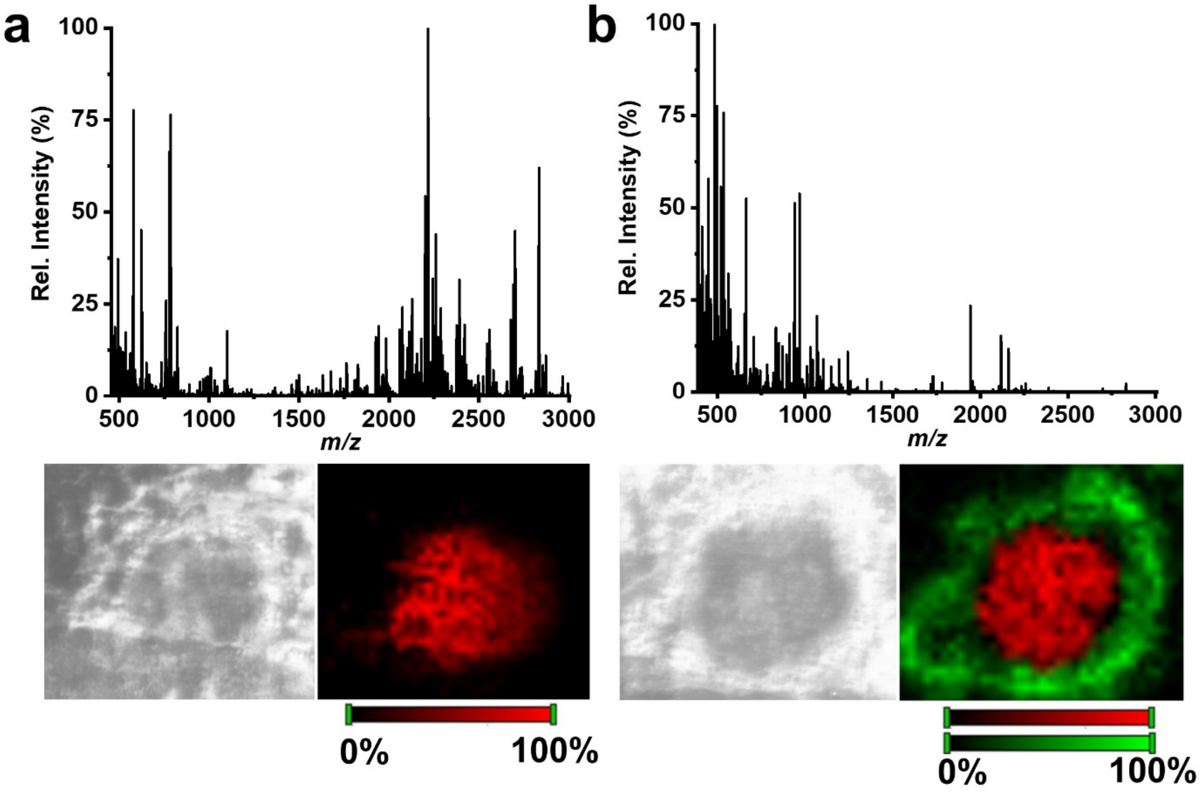

Figure S4. MALDI-MSI of soybean root nodule tissue sections infected with wild-type *B. japonicum* and sprayed with 9-AA containing salt additives using an oscillating capillary nebulizer. Top panel shows MALDI spectra averaged over entire tissue sections in (a) positive and (b) negative ion mode. Peaks corresponding to PHB oligomers are missing in both spectra. Bottom panel shows optical images of the tissue sections prior to MALDI imaging and chemical images for (a) an unknown ion at *m/z* = 2217.1645 that is localized exclusively in the infection zone (where PHB oligomers have been shown to localize), and (b) $[PE(32:5)+K-2H]^-$ (red) and $(\text{soyasaponin II}-H)^-$ (green).

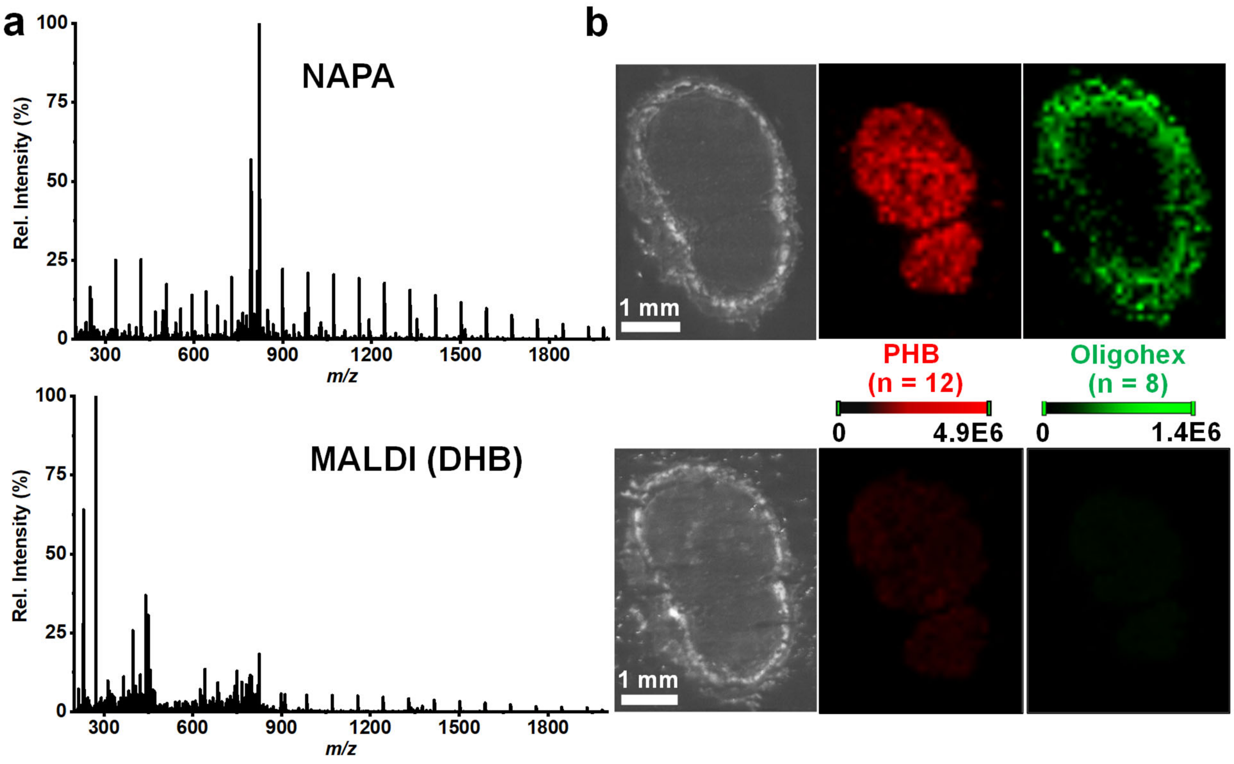

Figure S5. Comparison between NAPA-LDI-MSI and MALDI-MSI of soybean root nodule sections infected with wild-type *B. japonicum*. (a) Spectral comparison of MS scans averaged across the entire tissue region obtained by NAPA-LDI-MSI (top panel) and MALDI-MSI by matrix sublimation (bottom panel). (b) Optical images (left column) of root nodule sections before analysis by NAPA-LDI-MSI (top panel) and MALDI-MSI with DHB sublimation (bottom panel). Middle and right columns show chemical images for an oligomer of PHB (n = 12) and oligohexose (n = 8), respectively, produced by NAPA-LDI-MSI (top panels) and MALDI-MSI with DHB sublimation (bottom panels). The ion intensities in both the NAPA and MALDI images are scaled to the values displayed on the corresponding color scales.

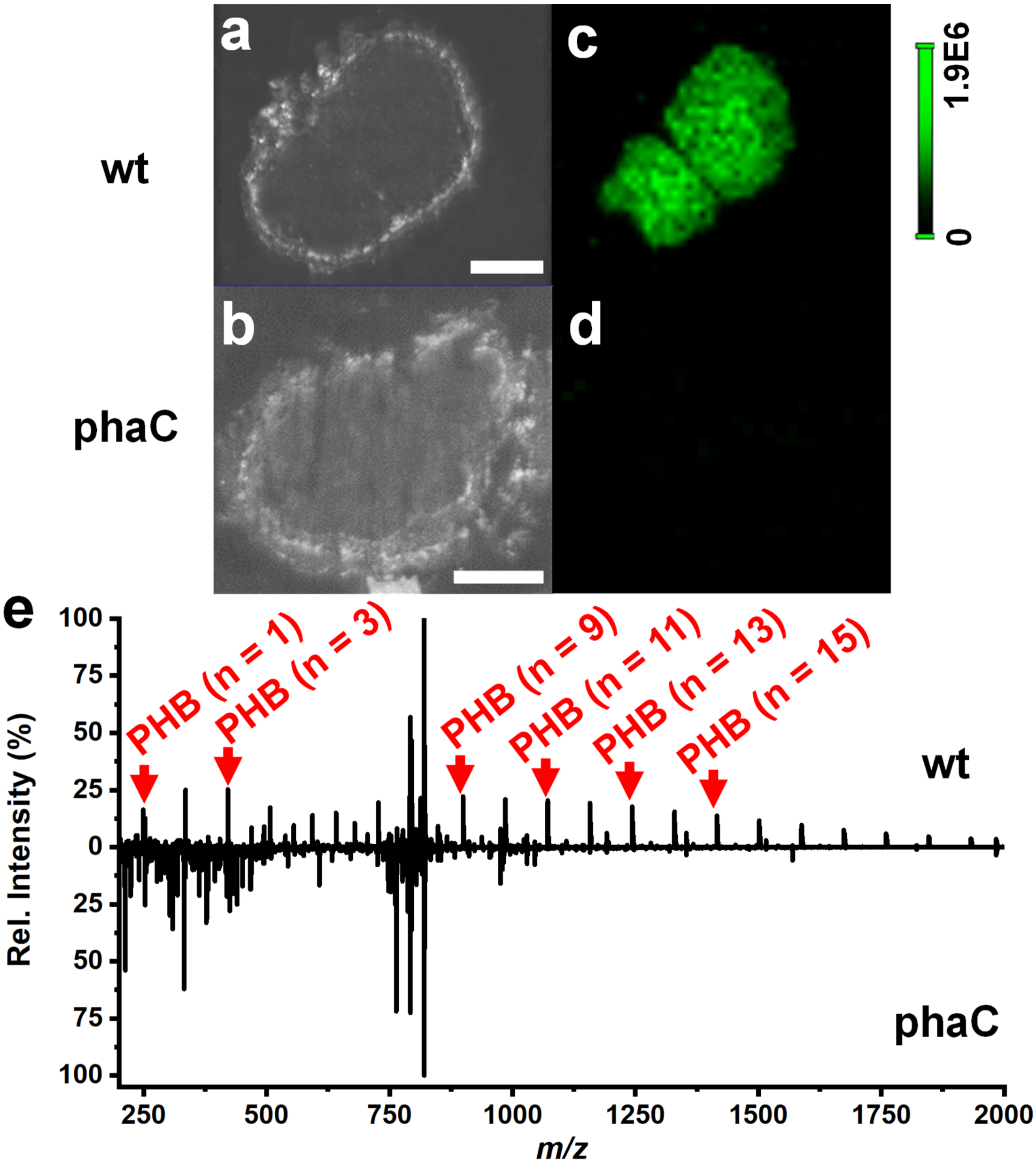

Figure S6. Comparison between NAPA-LDI-MSI of soybean root nodule sections infected with wild-type vs. *phaC B. japonicum*. Optical images of 10 µm sections from soybean root nodules infected with a) wild-type and b) *phaC B. japonicum*. Chemical images for PHB oligomer (n = 9) (*m/z* 899.3353) produced by NAPA-LDI-MSI of root nodule sections infected with c) wild-type and d) *phaC B. japonicum.* e) Spectral comparison of NAPA-LDI-MSI scans averaged across the entire tissue region in the two different samples. The ion intensities in both images are scaled to the values displayed on the color scale. Scale bars = 1 mm.

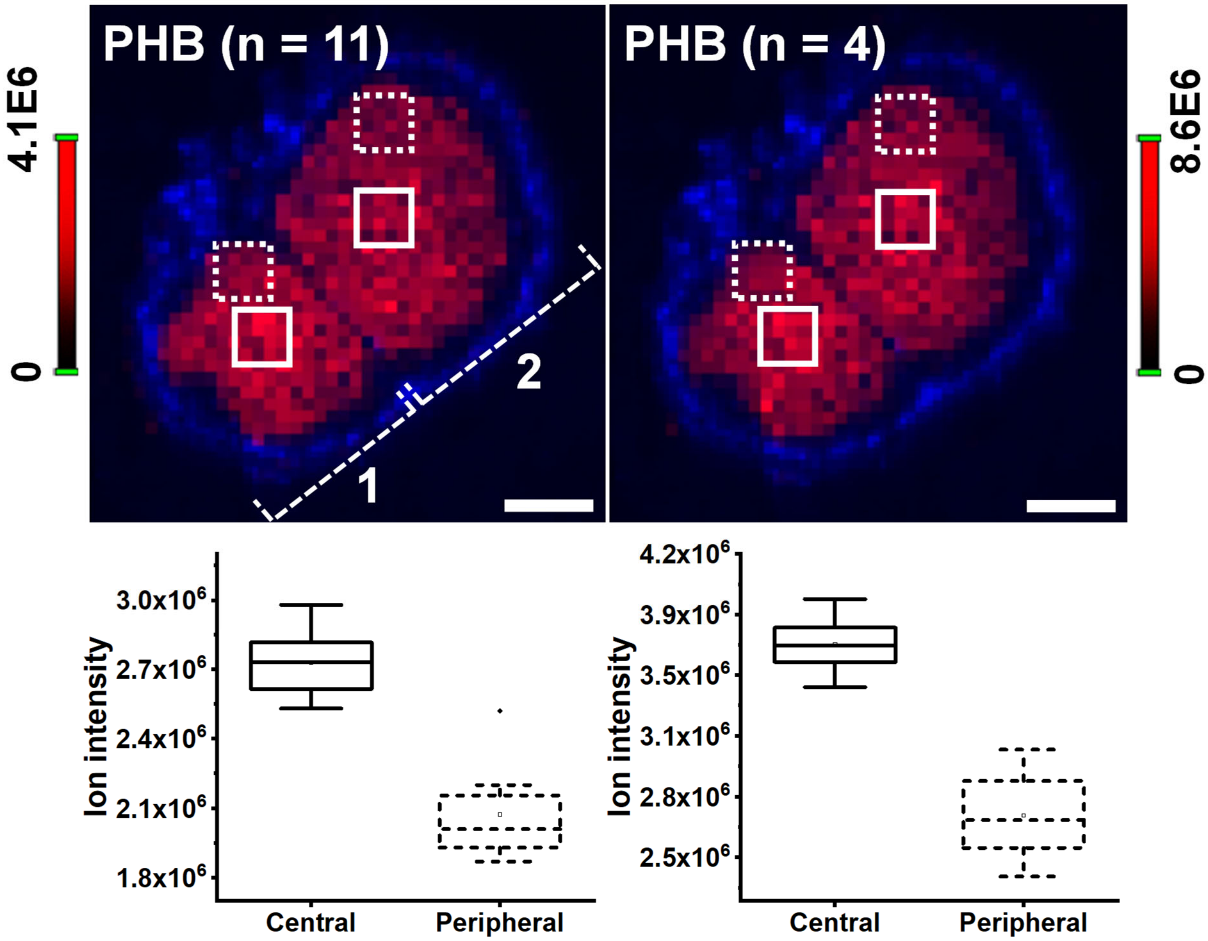

Figure S7. Heterogeneity of spatial distributions for 2 PHB oligomers (n = 11 and n = 4) in infection zone of root nodule tissue sections analyzed by NAPA-LDI-MSI. The top chemical images display the spatial distributions for PHB (n = 11) and PHB (n = 4) in the same tissue section taken from two conjoined root nodules (labeled ‘1’ and ‘2’). Optical image of the outer cortex is colored in blue. The bottom box-and-whisker plots compare the average ion intensities for PHB (n = 11) (left) and PHB (n = 4) (right) in the central (white box) and peripheral (white dashed box) regions of the infection zones measured in 8 serial root nodule tissue sections.

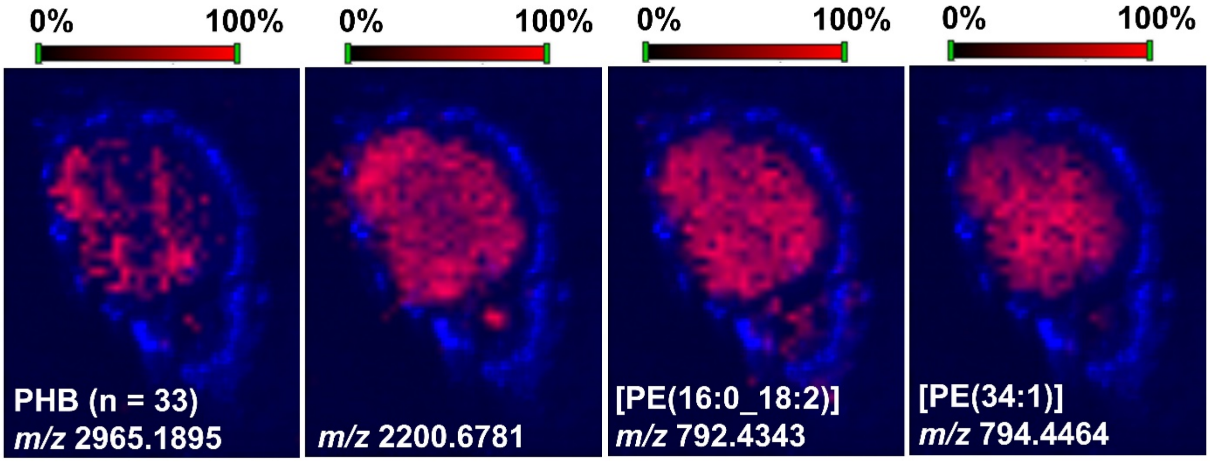

Figure S8. Comparison of spatial distributions of PHB (n = 33, *m/z* 2965.1895), an unknown ion at *m/z* 2200.6781, $[PE(16:0\_18:2)+2K-H]^+$ at *m/z* 792.4343, and $[PE(34:1)+2K-H]^+$ at *m/z* 794.4464 produced by NAPA-MSI in a tissue section.

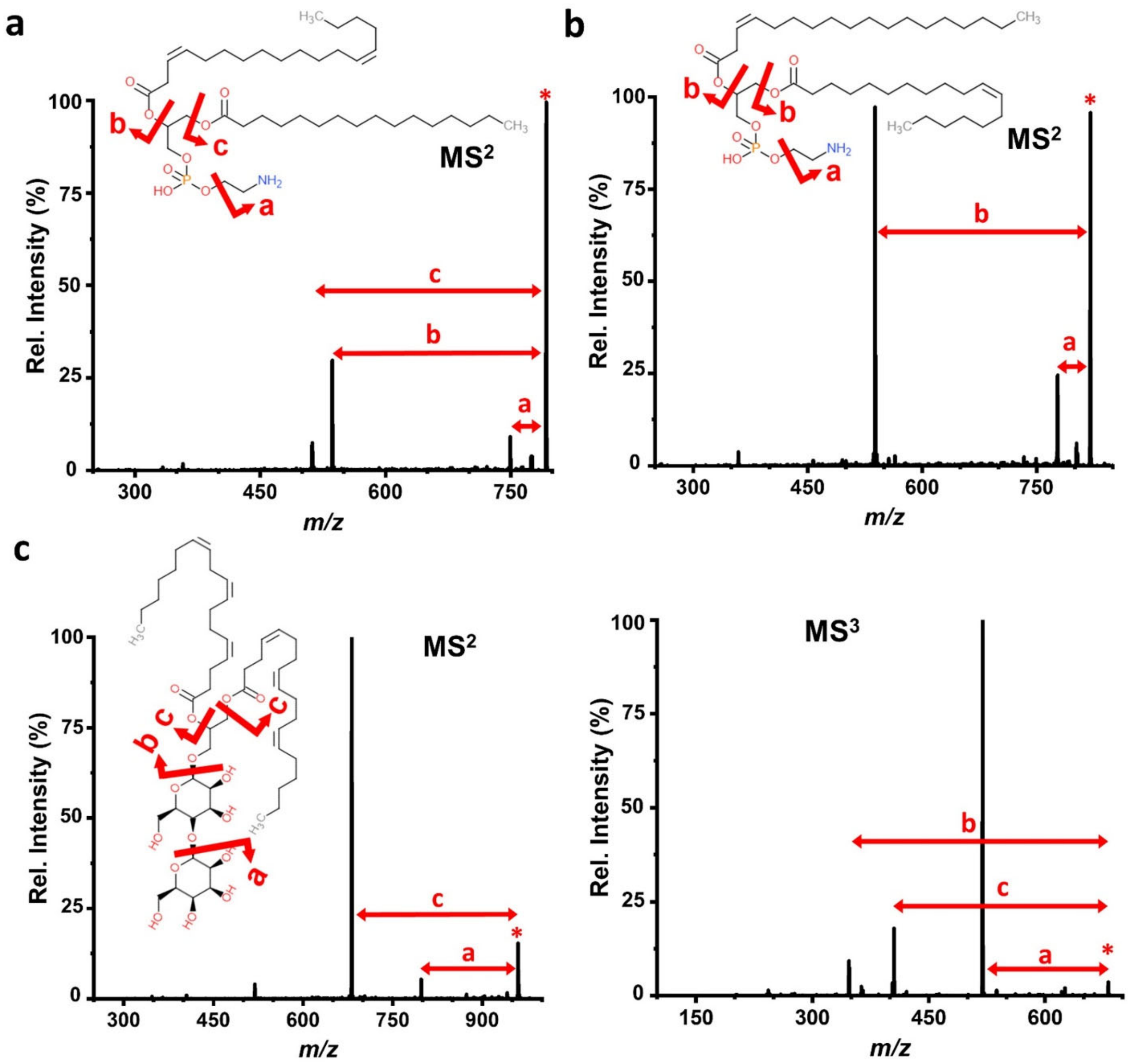

Figure S9. Identification of fatty acids, degree of unsaturation, and head groups for three lipids from soybean root nodules infected with wild-type *B. japonicum* using NAPA-LDI-MS^2 and -MS^3. NAPA-LDI-MS^2 of a) [PE(16:0_18:2)+2K−H]$^+$ (*m/z* 792.4343), b) [PE(18:1_18:1)+2K−H]$^+$ (*m/z* 820.4695), and c) [DGDG(18:3_18:3)+Na]$^+$ (*m/z* 959.5734) (left panel). NAPA-LDI-MS^3 of [DGDG(18:3_18:3)+Na]$^+$ is shown in the right panel, where the precursor ion corresponds to the base peak in the MS^2 spectrum in the left panel. The sn-isomerism, E/Z isomerism, and double bond positions in the fatty acid chains were not verified but are shown here to represent the fragmentations that are consistent with the observed MS^2 and MS^3 spectra.

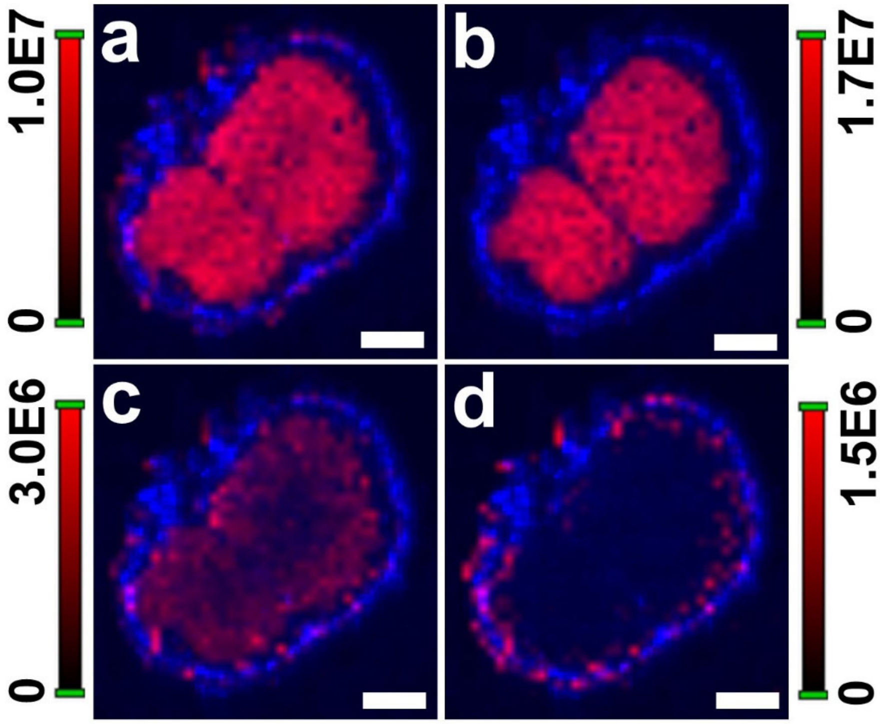

Figure S10. NAPA-LDI-MS images for four lipid ions in the same analyzed soybean root nodule tissue section infected by wild-type *B. japonicum*. Spatial distributions for a) $[PE(16:0\_18:2)+2K-H]^+$ (*m/z* 792.4343), b) $[PE(18:1\_18:1)+2K-H]^+$ (*m/z* 820.4695), c) $[DGDG(34:3)+K]^+$ (*m/z* 975.5467), and d) $[DGDG(18:3\_18:3)+Na]^+$ (*m/z* 959.5734). Optical image of tissue section is false colored in blue. Scale bars = 1 mm.

	NAPA	**MALDI (DHB)**	**Vendor data**[a]
M_n **(Da)**	1206	1584	2000
M_w **(Da)**	1573	1992	$2200 \leq M_w \leq 2800$
$Đ$ (M_w/M_n)	1.30	1.26	$1.1 \leq Đ \leq 1.4$

[a] Values provided by vendor are based on GPC measurements.

Table S1. Number- and weight-average molar masses and polydispersity data for a PHB standard recorded by NAPA-LDI-MS and MALDI-MS and the corresponding vendor specified values.

References

[1] N. J. Morris, H. Anderson, B. Thibeault, A. Vertes, M. J. Powell, T. T. Razunguzwa, *Rsc Advances* **2015**, *5*, 72051-72057.

[2] S. A. Stopka, C. Rong, A. R. Korte, S. Yadavilli, J. Nazarian, T. T. Razunguzwa, N. J. Morris, A. Vertes, *Angewandte Chemie International Edition* **2016**, *55*, 4482-4486.

[3] K. A. Saeed, F. O. Ayorinde, B. E. Eribo, M. Gordon, L. Collier, *Rapid Communications in Mass Spectrometry* **1999**, *13*, 1951-1957.

[4] X. D. Tang, P. A. Dreifuss, A. Vertes, *Rapid Communications in Mass Spectrometry* **1995**, *9*, 1141-1147.

[5] L. Z. Samarah, R. Khattar, T. H. Tran, S. A. Stopka, C. A. Brantner, P. Parlanti, D. Velickovic, J. B. Shaw, B. J. Agtuca, G. Stacey, L. Pasa-Tolic, N. Tolic, C. R. Anderton, A. Vertes, *Analytical Chemistry* **2020**, *92*, 7289-7298.

[6] J. I. Quelas, E. J. Mongiardini, J. Perez-Gimenez, G. Parisi, A. R. Lodeiro, *Journal of Bacteriology* **2013**, *195*, 3145-3155.

[7] W. J. Broughton, M. J. Dilworth, *Biochemical Journal* **1971**, *125*, 1075-1080.

[8] J. A. Fincher, J. E. Dyer, A. R. Korte, S. Yadavilli, N. J. Morris, A. Vertes, *Journal of Comparative Neurology* **2019**, *527*, 2101-2121.

[9] J. A. Fincher, A. R. Korte, S. Yadavilli, N. J. Morris, A. Vertes, *The Analyst* **2020**, DOI:10.1039/d1030an00836b.